Soft Matter

Cite this: *Soft Matter*, 2011, **7**, 7663

www.rsc.org/softmatter

PAPER

Adsorption of core-shell nanoparticles at liquid–liquid interfaces†

Lucio Isa,*[a] Esther Amstad,[a] Konrad Schwenke,[b] Emanuela Del Gado,[b] Patrick Ilg,[c] Martin Kröger[c] and Erik Reimhult[ad]

Received 8th March 2011, Accepted 11th May 2011
DOI: 10.1039/c1sm05407d

The use of nanoparticles as building blocks for the self-assembly of functional materials has been rapidly increasing in recent years. In particular, two-dimensional materials can be effectively self-assembled at liquid interfaces thanks to particle localization and mobility at the interface in combination with tailoring of specific interactions. Many recent advances have been made in the understanding of the adsorption and assembly at liquid interfaces of small hydrophobic nanoparticles stabilized by short-chain rigid dispersants but the corresponding studies on core-shell nanoparticles sterically stabilized by extended hydrophilic polymer brushes are presently missing. Such particles offer significant advantages in terms of fabrication of functional, responsive and bio-compatible materials. We present here a combination of experimental and numerical data together with an intuitive and simple model aimed at elucidating the mechanisms governing the adsorption of iron oxide nanparticles (5–10 nm) stabilized by low molecular weight poly(ethylene glycol) (1.5–10 kDa). We show that the adsorption dynamics and the structure of the final assembly depend on the free energy of the particles at the interface and discuss the thermodynamics of the adsorption in terms of the polymer solubility in each phase.

1 Introduction

The extraordinary properties of inorganic nanoparticles (NPs) are exploited in an increasing number of technological applications, including biosensing,[1] therapeutics[2–5] and diagnostics.[3,6] NPs can also be used as "additives" to improve the performance of existing materials[7] (*e.g.* thermal conductivity,[8] mechanical stability[9] or energy transfer[9]), or to impart new functions to them (*e.g.* magnetic[10,11] or triggered release[12,13]). In parallel, vast efforts have been recently made in order to synthesize and fabricate NPs of controlled shape and functionality[14,15] and to understand how they interact[16] with the aim to direct their assembly into complex structures.[17]

A particularly suited way to assemble NPs in a controlled way is to exploit their self-assembly at liquid–liquid or liquid–air interfaces (SALI).[18] Surface-active NPs adsorb and localize at interfaces, thus offering the possibility of easily assembling two-dimensional (2-D) materials for the fabrication of capsules,[19] ultra-thin cross-linked membranes[20–24] and free-standing metal films.[25] The reason for particle trapping at liquid–liquid interfaces has been extensively discussed in the literature[26,27] and hinges upon a free energy gain for the system due to the removal of interfacial area between two fluids when a particle resides at the interface.[28] The energy gain depends on particle size and wetting properties and on the interfacial tension between the two phases γ_0. Neutrally wetting conditions lead to the highest adsorption energy since they maximize the particle cross-sectional area at the interface. For this reason several strategies have been developed to tune the wettability of NPs, either by exchanging ligands on the particle to achieve the right surface chemistry,[19] by changing the solvent composition (*e.g.* by adding ethanol)[25,29] or by controlling the pH.[30] Despite vertical trapping at the interface, NPs still retain lateral mobility which, under the right circumstances, allows for the assembly of highly spatially uniform structures.[31,32] Moreover, at the interface additional inter-particle interactions are present,[27,33,34] *i.e.* electrostatic, capillary and solvation, which are absent in the bulk and which contribute to determine the structure of interfacial assemblies. All the aforementioned points highlight the flexibility of SALI as a route to fabricate 2-D NP-based materials. Of particular interest is to obtain 2-D materials with controlled NP content and spatial organization. In this respect, the use of expanded, solvated shells makes it also possible to assemble responsive membranous materials, for which the

[a]*Laboratory for Surface Science and Technology, Department of Materials, ETH Zürich, Wolfgang-Pauli-Strasse 10, 8093 Zürich, Switzerland. E-mail: lucio.isa@mat.ethz.ch; Fax: +41 (0)44 633 10 27; Tel: +41 44 633 63 76*
[b]*Microstructure and Rheology, Institute for Building Materials, Department of Civil, Geomatic and Environmental Engineering, ETH Zürich, Schafmattstrasse 6, 8093 Zürich, Switzerland*
[c]*Polymer Physics, Department of Materials, ETH Zürich, Wolfgang-Pauli-Strasse 10, 8093 Zürich, Switzerland*
[d]*Department of NanoBiotechnology, University of Natural Resources and Life Sciences (BOKU) Vienna, Muthgasse 11, 1190 Vienna, Austria*
† Electronic supplementary information (ESI) available: ESI contains an .avi movie of a pendant drop tensiometry experiment and additional QCM-D and numerical simulation data. See DOI: 10.1039/c1sm05407d

polymer matrix, the NP internal structure and inter-particle distance can be controlled over a large range of distances by applying external stimuli. Such membranes enable the true combination of the best features of polymer chemistry and physical properties of NPs. Moreover, many well-studied polymer brushes are hydrophilic and exhibit controlled biomolecular interactions; for these reasons such materials are highly relevant for biomedical and biotechnological applications.

Experimental studies on NP-SALI have almost exclusively dealt with "hard" NPs, stabilized by short chain, rigid dispersants. Most of these systems consist of hydrophobic particles modified by alkyl self-assembled monolayers. The most advanced examples have been demonstrated by Emrick, Russell and co-workers[20,35] and Möhwald and co-workers.[19,36] However, the unknown stability of the dispersant anchoring groups at the interface combined with limited hydrophobic shell thickness and homogeneity is likely to lead to aggregation at the oil–water interface and precludes the possibility of obtaining particle spacings larger than 1–2 nm. Regarding water soluble NPs, the very limited available examples include 2 nm Au NPs functionalized with short chain alkyl-oligo(ethylene glycol) thiols,[23] 8–40 nm charge-stabilized, citrate-capped Au NPs[29] and tobacco mosaic virus.[37] However, in the first case the use of only four ethylene glycol units led to weak stability and very short inter-particle separations. Citrate NPs were found to aggregate in 2-D domains and the charge stabilization was not sufficient to produce homogeneous monolayers as in the case of larger colloids.[28] Finally, virus particles offer tremendous monodispersity, shape and functional control as well as high structural order,[22] but do not possess the chemical or physical (optical, magnetic, mechanical) properties to perform the functions offered by inorganic nano-sized objects.

The limitations put forth above can be overcome by using core-shell NPs, where the shell comprises grafted, osmotically repulsive, hydrophilic polymers of controlled molecular weight (Fig. 1). The presence of the polymer shell has multiple functions. It above all provides colloidal stability to the particles in the aqueous phase. For this purpose it is crucially important that the polymer is irreversibly grafted to the particle cores at high density *via* a suitable anchoring group. The thickness of the polymer shell also determines the separation between the particle cores in close-packed assemblies. Moreover, the free end of the polymers can be functionalized to carry specific binding or cross-linking groups for targeting or *in situ* polymerization and dyes for fluorescent tagging. Finally, the choice of polymers responsive to external stimuli (*e.g.* temperature or pH) can be exploited to actuate the assembled structures.

In addition to application-driven advantages, SALI of core-shell NPs presents questions of high fundamental scientific interest. In core-shell NP-SALI the lowering of the interfacial energy by particle adsorption no longer depends only on the size and wetting properties of the core but also on the solubility of the organic polymer shell in the two solvents. The study of these effects is in its infancy. Numerical simulations have started to address the shell conformation for individual particles at liquid–liquid interfaces, but the studies are still limited to relatively short dispersants.[38,39] Preliminary experimental studies have highlighted a link between polymer molecular weight and colloidal stability at the interface.[40]

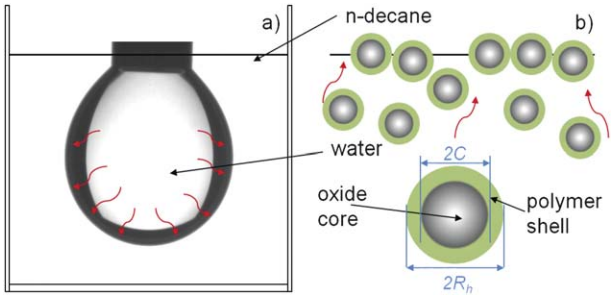

Fig. 1 Schematic representation of the pendant drop geometry (a) and of the adsorption process for core-shell NPs (b). The red arrows schematically represent diffusion of NPs from the bulk aqueous phase towards the liquid–liquid interface. NP core (C) and hydrodynamic radius (R_h) in water are highlighted. Upon reaching the interface, the NPs are adsorbed and their separation at close packing is determined by the thickness of the hydrated polymer shell, as it will be discussed further in the text.

We focus here on SALI of iron oxide NPs, which find numerous applications due to their magnetic properties and good biocompatibility,[41] including diagnostics[42] and therapeutics, *e.g.* hyperthermia.[4,5] Single-core iron oxide NPs can be sterically stabilized by a dense poly(ethylene glycol) (PEG) shell bound to the NP surface by a stable anchor *via* a simple "grafting to" approach.[43–47] We have recently demonstrated that particles of superior stability are obtained using PEG anchored with nitrocatechols[43,48] and thus all the results shown in this paper were obtained using Fe_3O_4 NPs stabilized by PEG-nitroDOPA shells of different thickness.

This work is triggered by the experimental observation of a complex adsorption behavior for iron oxide-PEG NPs at the water/n-decane interface (Fig. 1). Based on such observation, we have developed a set of experiments, simulations and theoretical models, which provide a comprehensive approach to decipher the adsorption behavior of soft sterically stabilized core-shell NPs. The experimental characterization is preceded by a short description of the particle synthesis and stabilization procedure. We later move to time-resolved interfacial tension measurements which capture the collective NP behavior at the interface and then attempt to gain microscopic insight by looking at the hydration of PEG brushes in the two solvents used. The "macroscopic-to-microscopic" approach is also followed in the presented numerical and modeling results, aimed at integrating and shedding light on the experimental data. Numerical studies unravel the different adsorption regimes as a function of particle interfacial binding energy and allow for the characterization of the interface coverage and the size distribution of adsorbed NPs. In addition to the collective NP adsorption behavior studied in the numerical simulations, we have also elaborated a simple theoretical model to explore further the effects of the polymer shell on the adsorption of individual NPs at liquid–liquid interfaces. The model is based on a Flory-type theory for a polymer brush grafted on a spherical colloid which sees an interface between two liquids with different qualities and gives as an output, aside from brush heights, the equilibrium position for a core-shell NP relative to the interface and corresponding free energy gain.

2 Results and discussion

2.1 Experimental results

2.1.1 PEG-iron oxide nanoparticles. Superparamagnetic iron oxide NPs were individually stabilized with PEG-nitroDOPA resulting in core-shell NPs. More details on the synthesis and stabilization protocols can be found in Section 3.1. Using an oil bath as an energy source, iron oxide NPs were nucleated and grown for 24 h under constant magnetic stirring at temperatures between 150 and 180 °C, depending on the targeted core size. Higher temperature results in larger particles. Directly after core synthesis PEG-nitroDOPA was grafted to as-synthesized NPs[49] (See Section 3.1 for details). The PEG molecular weight of PEG-nitroDOPA was varied between 1.5 and 10 kDa. The hydrodynamic size of core-shell NPs could be closely controlled by independently tuning the core size through the NP synthesis temperature and the shell thickness through the PEG molecular weight (M_w). This opens up the possibility of controlling independently the iron content and the separation between cores in a close-packed 2-D assembly. The size distribution of the cores (radius C) was characterized by transmission electron microscopy (TEM), small angle X-ray (SAXS) and neutron scattering (SANS). The mean hydrodynamic radius (R_h) of the core-shell particles, averaged over several batches, was measured by dynamic light scattering. The average size and standard deviation calculated over several batches are reported in Table 1. SANS and SAXS data could be fitted by assuming a log-normal core size distribution with a standard deviation of 0.3. The main causes of polydispersity are the variation in the core size from synthesis and the specific polymer shell conformation on each particle. Preliminary TGA (Thermo-Gravimetric Analysis) and SANS data indicate a packing density of PEG chains on the NP core surface ranging from 1 to 2 molecules/nm^2 with only a weak dependence on PEG M_w and core radius.

2.1.2 Interfacial tension measurements: Pendant drop tensiometry. In pendant drop tensiometry (PDT) the interfacial tension γ between two fluids is measured by imaging a droplet of one fluid phase immersed in the second one (Fig. 1). The drop profile is automatically detected and fitted with the Young-Laplace equation, extracting the value of γ.[50] In our case drops of aqueous NP suspensions are formed in n-decane and the interfacial tension is measured as a function of time; adsorption of NPs at the liquid–liquid interface lowers the system free energy which translates into an effective interfacial tension reduction, therefore by monitoring γ as a function of time we can obtain information about the adsorption kinetics.

Fig. 2 shows the normalized interfacial tension $\gamma' = \gamma/\gamma_0$ as a function of time for two iron oxide core sizes and three PEG molecular weights, where $\gamma_0 = 53.2$ mN m^{-1} is the interfacial tension of the pure water/n-decane interface.[51] Analogously to what was reported in preliminary studies,[40,52] we observe that the bulk concentration c and the PEG molecular weight have a strong influence on the adsorption kinetics. As the concentration of the NP suspension increases we observe that the initial value of γ' decreases; this is due to the fact that as the droplet is formed, a given number of particles (increasing with concentration) is already adsorbed at the interface leading to a value of $\gamma < \gamma_0$ above a size-dependent bulk concentration. Additionally, we observe that the interfacial tension decreases faster for more concentrated suspensions. This is expected as the adsorption rate scales with bulk concentration. Moreover, for all particles γ' plateaus (more or less markedly depending on the size) at high concentrations and long times to a saturation value γ_∞ which is independent of c. But what perhaps is the most striking feature of Fig. 2 is the complex shape of the time dependence of γ', which appears to be an exclusive of core-shell NPs. Such complex behavior is absent for "harder" objects which show a smooth γ decay with time.[53,54] Upon increasing particle size and bulk concentration, different adsorption regimes appear. Starting from the smallest particles with core radius $C = 2.1$ nm and stabilized by PEG 1500, we observe that by the increasing bulk concentration c, the γ' *versus* time curve initially decays smoothly ($c < 1 \times 10^{-6}$ mol) but then develops shoulders which correspond to transitions in the adsorption rates. A similar but more pronounced behavior is observed for the PEG molecular weight and larger core radius $C = 4.8$ nm. As the thickness of the PEG shell increases and thus the size of the NPs, the presence of a plateau in γ' at intermediate times becomes evident. Moreover with increasing c the plateau shows up at increasingly shorter times and for the highest concentrations a second, long-time plateau is observed. The latter also manifests itself at shorter times for higher concentrations and the value of the long-time, asymptotic interfacial tension γ_∞ becomes independent of c, corresponding to a saturation of the interface. The numerical simulations reported in Section 2.2 have the specific aim to elucidate further the nature of these complex adsorption regimes.

In order to exclude the possibility that the reduction in the interfacial tension is coming from free polymer and to confirm that the complex adsorption behavior is stemming from the presence of composite, soft NPs, we have also performed PDT experiments on pure PEG aqueous solutions. Fig. 3 shows γ as a function of time for NPs coated by PEG 5000 and $C = 2.1$ and 4.8 nm and for free PEG 5000 chains. At the concentration used ($c = 1 \times 10^{-5}$ mol) the free polymer very rapidly saturates the water/n-decane interface while the core-shell NPs show the complex behavior reported in Fig. 2. The PEG molecular weight has a strong influence on the asymptotic long-time interfacial tension γ_∞^{fpc} of the free polymer chains (fpc) (inset to Fig. 3), while this dependence is not observed for the core-shell NPs.

2.1.3 Polymer shell hydration: Quartz crystal microbalance. Quartz Crystal Microbalance with Dissipation (QCM-D)[55] is a sensitive technique to measure the hydration of planar thin

Table 1 Sizes of the iron oxide-PEG nanoparticles used in this work. The errors are standard deviations obtained comparing several particle batches

PEG molecular weight (M_w/kDa]	Synthesis temperature (T/°C)	Core radius (C/nm)	Hydrodynamic radius (R_h/nm)
1.5	150	2.1 ± 0.1	10 ± 2.5
5	150	2.1 ± 0.1	13 ± 3
10	150	2.1 ± 0.1	14 ± 2
1.5	180	4.8 ± 0.3	12 ± 1
5	180	4.8 ± 0.3	14 ± 2.5
10	180	4.8 ± 0.3	16 ± 2.5

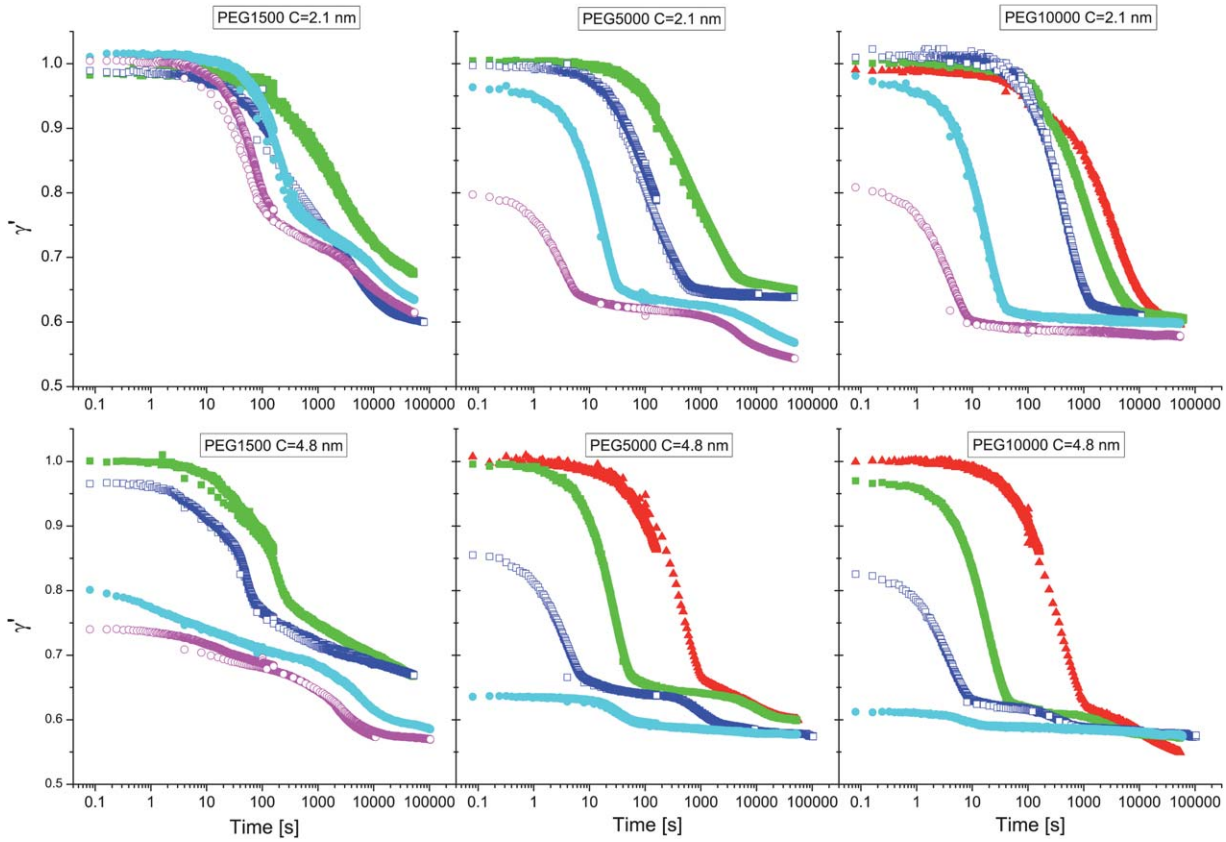

Fig. 2 Normalized interfacial tension $\gamma' \equiv \gamma/\gamma_0$ *versus* time at the water n-decane interface for particles of various PEG molecular weights and core sizes. The different symbols indicate the following concentrations on NP aqueous suspensions: (filled triangle) 2×10^{-7} mol; (filled square) 1×10^{-6} mol; (open square) 2×10^{-6} mol; (filled circle) 1×10^{-5} mol; (open circle) 2×10^{-5} mol.

films of known polymer density[56] *via* the monitoring of the shift of resonance frequency Δf, corresponding to film mass, and energy dissipation D, corresponding to viscous and hydrodynamic losses, of an oscillating quartz crystal. PEG-nitroDOPA

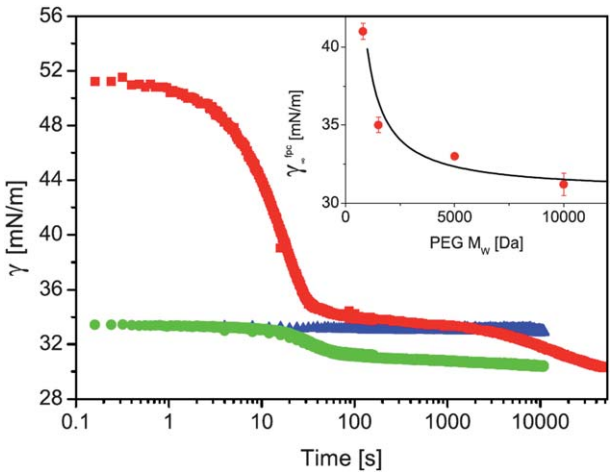

Fig. 3 Interfacial tension γ *versus* time at the water n-decane interface for particles coated by PEG 5000 with $C = 2.1$ nm (red squares) and $C = 4.8$ nm (green filled circles) and of non-tethered PEG 5000 (blue triangles) at 1×10^{-5} mol concentration (particles and free polymer chains, respectively). Inset: long-time interfacial tension γ_∞^{fpc} of the free polymer chains (fpc) *versus* PEG molecular weight at the water n-decane interface. The solid line is a fit from eqn (8) with eqn (7).

of the same molecular weights used to stabilize the NPs (1.5, 5 and 10 kDa) was adsorbed *ex-situ* on TiO_2 coated QCM-D crystals.‡ The hydration change in the brushes upon exposing them to water and n-decane was then measured. The raw data are summarized in Fig. 4. We initially measured a baseline at 25 °C in Millipore water where the PEG brush is fully hydrated and subsequently exchanged the solvent with n-decane at $t = 30$ min. Upon solvent exchange an increase in the resonance frequency of the crystals was measured, accompanied by a reduction in the dissipation. Since control measurements on bare TiO_2 showed the baseline shifts to be insignificant when water was exchanged for n-decane (see ESI†), these two observations can be ascribed to a partial collapse of the polymer brush. The positive frequency shift is interpreted as a reduction of the brush hydrated mass as the thickness of the brush is reduced and liquid mass is expelled from it.[56] Analogously the dissipation decreases as viscous losses from fluid motion within the brush are reduced.[58,59] The brushes could easily be rehydrated and re-expanded to their original thickness as demonstrated by the return to the baseline values when the n-decane was replaced again by water at $t = 90$ min.

To quantify the amount of collapse it is also necessary to measure the absolute hydrated mass of the PEG-nitroDOPA films. However, the protocol for functionalization of TiO_2 surfaces with a stable PEG brush cannot be performed *in situ* in

‡ Nitrocatechol-PEG in this molecular weight range has been shown to form brushes when adsorbed on TiO_2.[57]

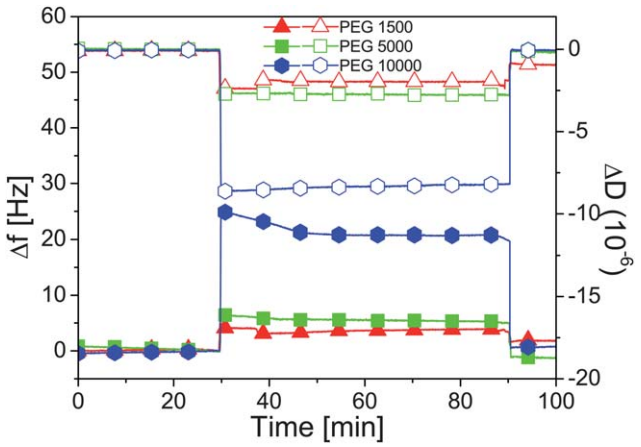

Fig. 4 Frequency shifts Δf (filled symbols) and dissipation ΔD (open symbols) measured with QCM-D as a function of time on adsorbed brushes of PEG-nitroDOPA of various molecular weights. At $t = 30$ min, Millipore water is exchanged with n-decane and we note the correspondent increase in Δf and decrease in ΔD stemming from partial collapse of the polymer chains. At $t = 90$ min, the solvent is changed back to Millipore water and the baselines are recovered showing the reversibility of the collapse.

our QCM-D setup (see Section 3.1 for details). Furthermore, the density and density profile of PEG brushes on the planar TiO_2 and on the Fe_3O_4 NP surfaces are expected to differ significantly.[57,12] A quantitative extension of the results presented here to the collapse of PEG shells on NPs at the water/n-decane interface is therefore not meaningful, but we nonetheless note that a significant collapse is observed in n-decane and that, as expected, the absolute collapse is higher for thicker brushes (higher PEG molecular weight). For these reasons we decided to carry out a modeling study which, upon the existence of the evidence of at least a partial collapse of the polymer shell, is aimed to elucidate the role that polymer solubility has on the free energy of individual core-shell NPs at liquid interfaces (Section 2.3).

2.2 Numerical simulations results

2.2.1 Model and simulations. We design a simple model, aimed at a first qualitative understanding of the basic mechanisms of the collective particle adsorption behavior at the interface. We consider the NPs as soft spheres interacting *via* the interaction potential $U_{ij}(r) = \varepsilon[(\sigma_i + \sigma_j)/r_{ij}]^{12}$, where σ_i denotes the radius of particle i, r_{ij} the distance between the centers of particles i and j and ε sets the energy scale. In the experimental system the particles interact *via* soft steric repulsion of the polymer shells; the experimentally determined thickness of the shell ensures that the range of steric repulsion is much greater than the range of attractive van der Waals interactions, with a high energy barrier to reach the inter-particle distances required for significant van der Waals attraction. Therefore, for simplicity, our effective potential only reflects the repulsive part of the interaction potential. In order to reproduce faithfully the nature of such interactions, one must know the details of the density profile of the polymer shell around the oxide cores, a complex task for objects with high curvature and roughness on the relevant nanoscale. $U_{ij}(r)$ represents the simplest choice from a numerical point of view to describe the inter-particle interactions and to account for the experimental features without introducing assumptions not verifiable here. To mimic the experimental system, we extract particles from a log-normal distribution of particle sizes with mean radius σ and standard deviation 0.3σ. In the following we will use σ as our unit length, ε the unit energy and m the mass of the particle. For practical purposes in the simulations we use a truncated distribution (*i.e.*, $\sigma_i > 0.9$ and $\sigma_i < 1.5$). Solvent molecules are not simulated explicitly since they are much smaller than the NPs and the interface is modeled *via* a 2-D simulation box of linear size $L = 80$ with periodic boundary conditions.

To adsorb/desorb particles we use a Grand-Canonical Monte Carlo (MC) scheme where the Metropolis rate is given by the energy difference upon adsorption/desorption of a particle randomly chosen from the distribution specified above, the temperature T and the number of adsorbed particles.[60] The energy gain for a particle i to be adsorbed onto the interface is taken to be $-\Delta E_i = \Delta E_0(\sigma_i/\sigma)^2$, where ΔE_0 is determined by the solvent pair (water/n-decane in this case), the particle surface chemistry and size.[28] Note that this expression assumes *naked* (non-coated) particles centered at the interface. The contribution of the core-shell nature of our NPs will be discussed in Section 2.3. The adsorption/desorption rates are fixed by ΔE_i, the number N of particles at the interface and the change ΔU_i in the interaction energy on the surface upon adsorption/desorption of particle i.[60] In the simulations we consider ΔE_0 from $1.0k_BT$ to $100k_BT$, where k_B is Boltzmann's constant; the experimental values for our system are higher (see Section 2.4), but $\Delta E_0 = 50k_BT$ already starts to capture some essential features of systems with irreversible adsorption at the interface over the simulation time window considered here.

We perform Δ steps of Molecular Dynamics (MD) between two MC cycles to mimic the particle dynamics at the interface, using velocity Verlet with a step 0.002 and fixing the temperature $T = 1.0$ *via* velocity rescaling.[61] The unit time is $t_0 = \sqrt{m4\sigma^2/\varepsilon}$. The data presented here correspond to $\Delta = 10$ MD steps. In the following, we use the MD time as the lapsing time of the numerical experiments and we qualitatively compare the different regimes detected in the simulations to the ones observed in the adsorption experiments. A quantitative matching of the numerical time with the physical time will be performed in future work.

Finally, we assume that the particle density close to the interface scales with the bulk concentration c. This corresponds to a higher rate of adsorption attempts (as described by the MC cycle). Hence, in a first simple approximation, in order to account for concentration effects, we consider each MC cycle to be limited to N_0 attempts and therefore assume an attempt rate N_0/Δ: increasing values of N_0 correspond to increasing concentration. Here we varied N_0 between 10 and 10^4.

2.2.2 Results. Using the procedure described above, we follow the adsorption process and monitor the progressive population of the interface as a function of the simulation time defined above. At each time t we calculate the surface coverage, *i.e.* the fraction of the simulation box occupied by the adsorbed particles $\Phi(t) = \sum_i \pi\sigma_i^2/L^2$ obtained by sampling the simulation

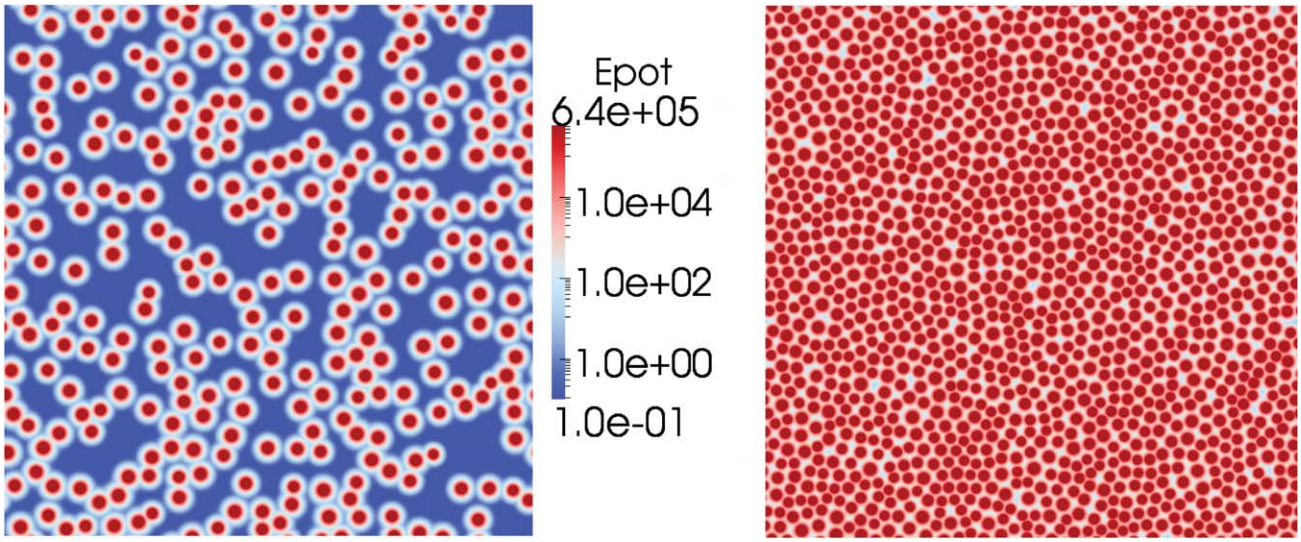

Fig. 5 Snapshots of the 2-D simulation box after 0.8 t_0 for $\Delta E_0 = 1k_BT$ (left) and $\Delta E_0 = 100k_BT$ (right), leading to a surface coverage Φ of $\simeq 0.26$ and $\simeq 0.8$, respectively. The color code indicates the potential energy.

box with a grid of 2500 points per unit area σ^2. With a fixed N_0 (*i.e.*, $N_0 = 10^3$), we observe that the adsorption process changes upon changing ΔE_0. Fig. 5 shows snapshots of the simulations, where a different surface coverage Φ between $\Delta E_0 = 1k_BT$ and $\Delta E_0 = 100k_BT$ is attained. Moreover it already suggests that also the size distribution of the two populations might be different.

The number and size of particles adsorbed at the interface determine the reduction of the interfacial tension; in particular, the normalized interfacial tension $\gamma' = \gamma/\gamma_0$ reported in Fig. 2 is linearly related to $\Phi(t)$ *via* eqn (6). Fig. 6 shows $1 - \Phi(t)$ as a function of time for different ΔE_0§. The surface coverage obtained at the end of the simulation increases monotonically upon increasing ΔE_0. For low adsorption energies $\Delta E_0 < 10k_BT$, the system reaches an equilibrium surface coverage over the simulation time window: particles are continuously adsorbed and desorbed but the surface coverage value does not change. The permanence time on the surface of a particle of $\sigma_i = 1.0\sigma$ is typically $\simeq 10t_0$ for $\Delta E_0 = 1k_BT$. The permanence time increases with ΔE_0 and at the largest ΔE_0 hardly any particle is desorbed; for $\Delta E_0 \gtrsim 20k_BT$, the adsorption curves show an evolution towards higher surface coverage without reaching a steady state within the simulation time frame.

An interesting feature of the curves in Fig. 6 which also appears in the experimental data, is the complex behavior of $1 - \Phi(t)$ at intermediate times ($\sim 0.2t_0 < t < 10t_0$) for the largest adsorption energies. The observed intermediate plateau in $1 - \Phi(t)$ corresponds to the fact that, after a first rapid filling of the surface, adsorption is blocked until a sufficiently large void becomes available. Once the particles which were adsorbed in the initial filling have had time to rearrange, particles equal to or smaller than the available void can be adsorbed and thus increase further the surface coverage. At small adsorption energies $\Delta E_0 \leq 1k_BT$ the system smoothly evolves towards its equilibrium distribution, with a progressive increase of the mean radius ($\langle\sigma(t)\rangle = \sum_i \sigma_i(t)/N$) and a corresponding decrease of the polydispersity ($\delta(t) = (\langle\sigma^2(t)\rangle - \langle\sigma(t)\rangle^2)/\langle\sigma(t)\rangle^2$, where $\langle\sigma^2(t)\rangle = \sum_i \sigma_i^2(t)/N$) at the interface towards "optimal" values where particles are continuously adsorbed and desorbed (Fig.7). For larger adsorption energies $10k_BT \gtrsim \Delta E_0 \gtrsim 20k_BT$, desorption events become rare and a new type of adsorption dynamics sets in: higher surface coverage is attained upon adsorbing relatively larger particles, as compared to the case of lower ΔE_0. The system eventually evolves towards the steady state upon decreasing the mean radius and polydispersity on the surface only at much longer times. Finally, for even larger adsorption energies $\Delta E_0 \gtrsim 50k_BT$, the system gets stuck in a regime characterized by the irreversible adsorption of particles of any size. The mean radius of the particles at the interface keeps decreasing due to the fact that at longer times only smaller and smaller particles can fill the space left by the irreversibly trapped particles and therefore the polydispersity does not decrease and

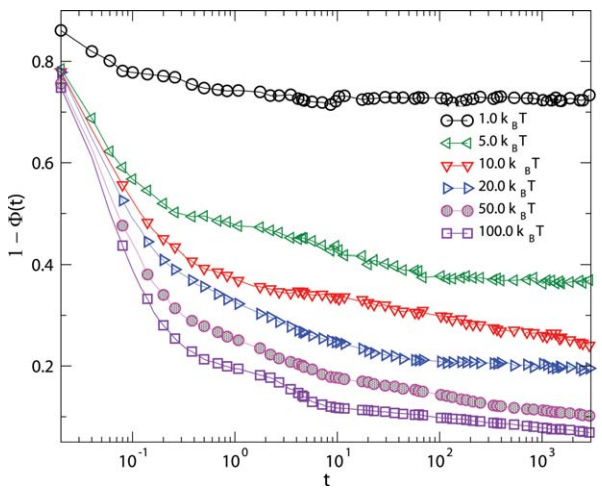

Fig. 6 $1 - \Phi$ (related to $\gamma' = \gamma/\gamma_0$ *via* eqn (6)) *versus* simulation time for different adsorption energy strengths ΔE_0 from numerical simulations of NP adsorption in the simulation box.

§ From eqn (6), it follows that $\gamma/\gamma_0 = 1 - \Phi$ only if one assumes $\gamma_0 = \Delta E/\pi\sigma^2$ but the shape of the curve is not affected by the choice of γ_0.

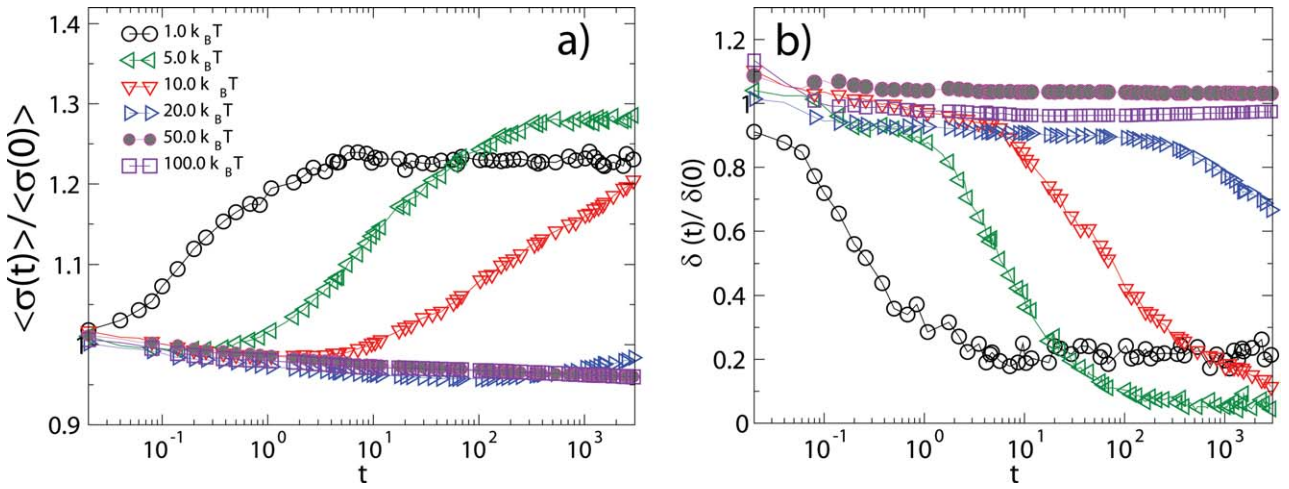

Fig. 7 Average size (a) and relative fluctuation (b) of the particle radius in the simulation box *versus* simulation time for different adsorption energy strengths ΔE_0 (here normalized with their initial values).

remains, in the simulations window, very different from the "optimal" values attained in the equilibrium regime of small ΔE_0.

These observations are summarized in Fig. 8. In particular we observe that the maximum attained NP surface coverage grows monotonically with ΔE_0 and so does the long-time polydispersity for large adsorption energies. For small adsorption energies ΔE_0 the adsorption process is dominated by the "optimal" size selection, which is more effective upon increasing ΔE_0, hence the final attained polydispersity accordingly decreases and is smaller than the one of the parent distribution. For large ΔE_0 instead, the adsorption dynamics is controlled by the persistence of larger particles at the interface and the irreversible progressive space filling which corresponds to a polydispersity close to the initial one.

To study the effect of bulk concentration of the initial NP suspension on the adsorption process, we fix $\Delta E_0 = 100 k_B T$ and vary N_0. In Fig. 9 we plot $1 - \Phi(t)$ as a function of time. The numerical data show remarkable similarities to the experimental findings. The short-time value of $1 - \Phi(t)$ decreases with increasing N_0, in agreement with the picture where a large number of particles is rapidly adsorbed in the first stages of the experiments at higher initial concentrations, as indicated by the decrease of the initial values of γ (Fig. 2). Moreover, for $N_0 \lesssim 10^2$ a lower surface coverage is obtained over the same simulation time window and $1 - \Phi(t)$ does not show the plateau discussed before. This is also qualitatively consistent with the experimental observations of Fig. 2 and suggests that, for sufficiently diluted suspensions, the adsorption kinetics leads to a continuous increase of the surface coverage without being much affected by the inter-particle interactions at the interface. For $N_0 \gtrsim 10^3$, we note the appearance of the adsorption plateau at intermediate times and a saturation value of the final coverage which is only weakly dependent on N_0 within the simulation time window, in analogy to what is reported in Fig. 2 as a function of the bulk concentration c.

Overall, in spite of the rather crude assumptions, the simple model and simulation approach described above seem to capture the qualitatively most striking features of the PDT experiments.

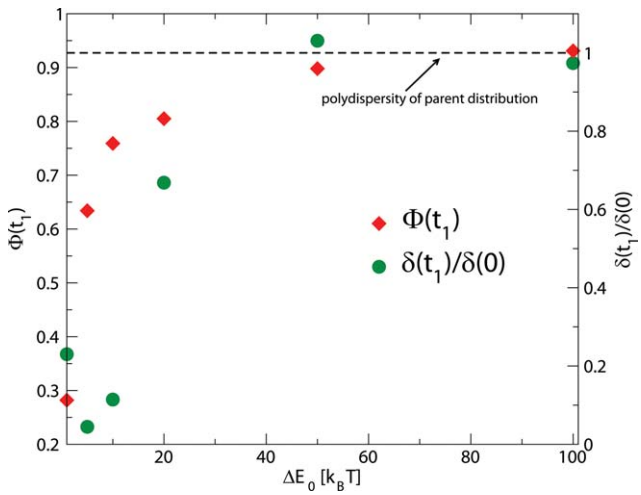

Fig. 8 Long-time interfacial surface coverage Φ (left axis) and polydispersity of the adsorbed particle distribution (right axis) extracted from simulations as a function of adsorption energy ΔE_0. The values refer to $t_1 \simeq 1.0 \times 10^3 \tau_0$.

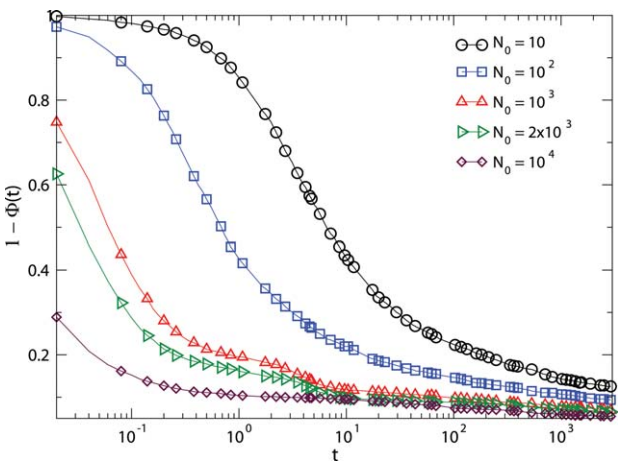

Fig. 9 $1 - \Phi$ as a function of simulation time for systems with a different number of attempts to adsorb/desorb particles and $\Delta E_0 = 100 k_B T$.

The results of the preliminary numerical studies presented here suggest that cooperative processes (*i.e.*, the creation of space sufficient for the adsorption of new particles) are relevant and significantly affect the adsorption kinetics.

However, a more detailed representation of the experimental system would take into account the active role played by the polymer shell in determining the position of the NP relative to the interface, the corresponding reduction of interfacial area and the binding energy. In the following we therefore propose a Flory-type theory to account for the effect of the liquid–liquid interface on the polymer chains attached to the surface of the colloidal particle.

2.3 Modeling results: a Flory-type theory for polymer brush on colloids at liquid–liquid interfaces

2.3.1 Energy of a polymer chain tethered to the surface of a colloid. In order to understand the behavior of core-shell NPs at the interface, let us first consider the case of a single polymer chain belonging to a brush tethered to the surface of a colloid immersed in a solvent. The free energy of the chain can be written as a sum of an entropic elasticity term and an interaction contribution between the chains in the brush, $f_i = f^{el} + f_i^{int}$. The label $i = 1, 2$ indicates the two liquids (solvents) at both sides of the interface (see Fig. 10).

A simple form of the elasticity entropy is given by $f^{el}(R)/k_BT = \frac{3}{2}[(R/R_0)^2 + (R_0/R)^2]$ as function of brush height R, where R_0 is the size of an ideal chain with N spherical monomers of size a. The molecular interpretation of these quantities depends on the polymer model used. We will later employ a wormlike chain model for quantitative comparisons with the experimental results.

In a mean-field approximation, the interaction between polymer chains is taken into account by[62,63]

$$f_i^{int}/k_BT = \frac{N}{\phi}[(1-\phi)\ln(1-\phi) + \chi_i\phi(1-\phi)], \qquad (1)$$

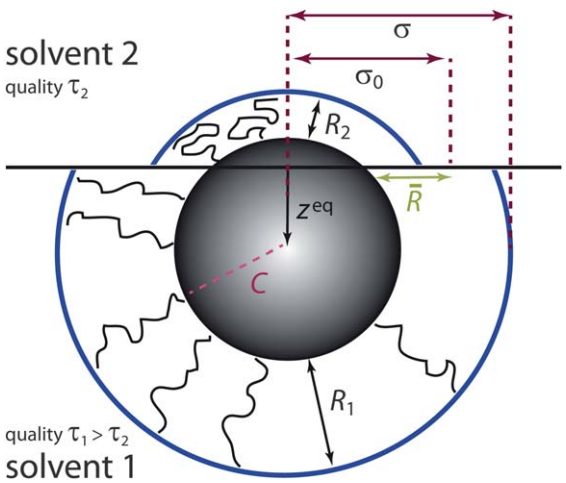

Fig. 10 Schematic representation of a core-shell NP at a liquid–liquid interface highlighting all the quantities necessary for the derivation of the theoretical model.

where $\phi = Na^3/V(R)$ is the volume fraction of the polymer in the brush and $V(R)$ the available volume for a partially confined chain of size R tethered to the colloid surface. The dimensionless Flory-Huggins interaction parameter χ_i, more conveniently replaced by $\tau_i = 1 - 2\chi_i$, depends on the solvent quality of liquid i: $\tau_i > 0$ corresponds to good solvent, while $\tau_i < 0$ describes poor solvent conditions. Typically, τ_i increases with increasing temperature. At the Θ-temperature, one has ideal solvent conditions, with $\tau = 0$. Assuming $\tau_1 > \tau_2$, the equilibrium polymer sizes R_i^{eq} are different in the two liquids and are calculated by minimizing the free energies $f_i(R)$ separately.

So far, we have followed the classical Flory theory in each solvent i for which the equilibrium polymer size R_{eq} in some simple geometries is known[63]¶. In the following, we extend the theory to a curved surface and consider additional contributions arising from the presence of a liquid–liquid interface. Our approach to describe the brush tethered to the NP core (also known as Alexander brush for the case of tethering to a planar surface,[62] *i.e.* infinite core) does not allow us to calculate the density profile within the polymer layer, or a corresponding effective interaction potential. The former can however be derived following the self-consistent field approach reviewed and extended to branched polymers in.[64] For the purpose of the following arguments, the precise knowledge of the density profile is not required.

2.3.2 Single core-shell nanoparticle. We can now calculate the contribution of the polymer shell to the free energy of a single NP at the interface using the expressions presented above. Let C denote the radius of the spherical NP core, z the height of its center relative to the liquid–liquid interface, and R_1 and R_2 the brush heights (shell thicknesses) in the two respective solvents (Fig. 10). In the case of a "naked" particle, the free energy contribution stemming from interfacial adsorption is $F_{12} = -\gamma_0 A_{12}(z)$, where γ_0 is the interfacial tension between the two fluids and $A_{12}(z)$ is the cross-sectional area occupied by the particle at a height z from the interface.[28] For a particle coated by a densely packed brush, $A_{12}(z)$is replaced by the area occupied by the core and shell $A_{12}(z,\bar{R}) = \pi[(C^2 - z^2)^{1/2} + \bar{R}]^2$ where, $\bar{R} \equiv (R_1 + R_2)/2$ is an effective shell thickness within the plane of the interface. The free energy contribution thus becomes $F_{12}(z) = -\gamma_0 A_{12}(z,\bar{R})$. Except for the interface region, the polymers contribute with a free energy f_i per chain, *i.e.* in total $n_1(z)f_1 + n_2(z)f_2$, where $n_i(z)$ is the number of polymers on the surface of the core exposed to solvent i. We have implicitly assumed that the chains are predominantly exposed to either solvent 1 or 2. This description becomes unsuitable in the limit of vanishing core, $C = 0$ (to be discussed separately below).

We assume homogeneous coating, where Σ is the area per polymer, *i.e.* the inverse grafting density. Given these approximations, the free energy of the coated NP at the interface is given by

$$F(z) = n_1(z)f_1(R_1^{eq}) + n_2(z)f_2(R_2^{eq}) - \gamma_0 A_{12}(z,\bar{R}_{eq}) \qquad (2)$$

¶ For the case of a planar brush, $V(R) \sim R$, while for a free polymer chain in solution, $V(R) \sim R^3$

As mentioned above, we obtain the equilibrium size of the polymer R_i^{eq} in the two solvents by minimizing separately $f_i(R)$. We thus assume that the polymer size is unaffected by the presence of the interface. We expect this to be a good approximation for dense brushes sufficiently far from the interface, but this becomes questionable close to the interface, where the shell can be deformed.[38,39] Moreover, the definition of an effective shell thickness $\bar{R}$ at the interface is also neglecting such shell deformations. For the minimization of $f_i(R)$, explicit expressions for the available volume are needed. By purely geometric arguments, the available volume per chain of given size R is $V(R) = \frac{4\pi}{3n}[(C+R)^3 - C^3]$. The total number of tethered chains is the sum $n = 4\pi C^2/\Sigma = n_1(z) + n_2(z)$ and, for homogeneous coating, the number of tethered polymers in solvent 1 and 2 is $n_1(z) = 2\pi C(C+z)/\Sigma$ and $n_2(z) = 2\pi C(C-z)/\Sigma$, respectively.

2.3.3 Effective particle size and interfacial tension. Having obtained the equilibrium polymer sizes R_i^{eq} in both liquids, their arithmetic mean, $\bar{R}_{eq} = (R_1^{eq} + R_2^{eq})/2$, is taken as the effective shell thickness at the interface (Fig. 10). Therefore the cross-sectional area taken up by a single particle at the interface‖ is $A_{12}(z,\bar{R}) = \pi\sigma_0^2$ with

$$\sigma_0 = (C^2 - z_{eq}^2)^{1/2} + \bar{R}_{eq}. \quad (3)$$

For particles sitting preferentially in the solvent with highest quality (1), σ_0 does not represent the true distance between the centers of two touching particles.** This distance is instead

$$\sigma = C + R_1^{eq}, \quad (4)$$

determined by the thickness of the brush at the NP equator buried in the water phase below the interface plane (see Fig. 10). This fact will have consequences on further refinements of our coarse–grained simulation model, since the length scale relevant to the adsorption energy is σ_0, while the inter-particle interactions are determined by σ. To highlight once more the difference between these two quantities it is worth pointing out that under very poor solvent conditions for solvent 2, σ_0 can also become smaller than C, loosing any physical meaning as inter-particle distance.

In order to compare these two distances, we need to minimize $F(z)$, eqn (2), with respect to z to obtain the equilibrium height z^{eq} of the coated NP center from the liquid–liquid interface. The maximum and minimum values of z^{eq} correspond to NPs that are fully immersed in solvent 1 and 2, respectively. An analytic expression for z^{eq} is not available in closed form and it has to be evaluated numerically.††

With all the relevant quantities at hand, the binding energy of a single core–shell NP coated by n chains is obtained as the difference between (i) the free energy at its equilibrium position z^{eq} within the interface, and (ii) the free energy of the same NP dissolved in the best of the two solvents,

$$\Delta E = F(z^{eq}) - nf_1(R_1^{eq})0, \quad \tau_1 > \tau_2 \quad (5)$$

with $F(z)$ according to eqn (2).

Given a macroscopic surface area δA, at saturation coverage Φ (we assume 2-D close-packing $\Phi = 0.91$ of equally-sized particles), the number of NPs at the interface is $\Phi\delta A/\pi\sigma^2$ and the related reduction of macroscopic surface tension is $-\Delta E$ times the number of NPs, divided by δA, in agreement with the approach of Du and co-workers.[54] Accordingly, we extract the asymptotic long-time interfacial tension γ_∞ (as measured in experiments) from the energy gain, eqn (5), and the equilibrium NP radius, eqn (4), *via*

$$\gamma_\infty = \gamma_0 + \frac{\Phi\Delta E}{\pi\sigma^2}, \quad \Delta E < 0. \quad (6)$$

2.3.4 Determination of theory parameters and results. We now come to the numerical estimations of the quantities of interest. The parameters needed for the Flory–type theory for free PEG chains are monomer size a, ideal chain size R_0, solvent qualities τ_i, and $N \approx 23M_w$/kDa for a given PEG molecular weight M_w. Adopting a wormlike chain model with $a = 0.32$ nm and persistence length $l_p = 2a$, the square radius of gyration is given by[65]

$$R_0^2 = \frac{2}{3}Na^2\left[1 - 3x + 6x^2 - 6x^3\left(1 - e^{-1/x}\right)\right], \quad (7)$$

with $x \equiv l_p/Na$. Despite the lack of agreement in the literature for the precise choice of these parameters,[65–67] using the figures reported above and $\tau_1 = 0.13$, the resulting equilibrium size R_0 is compatible with the hydrodynamic radii reported in[68] for PEG in water (*cf.* values for R_1^{eq} in Table 2).

The model is also able to predict the size, free energy gain and corresponding interfacial tension reduction for single free polymer chains (fpc) at the interface. A single chain of size R gains, when absorbed at the interface, an amount of free energy that is proportional to the area occupied by its N monomers, $\Delta F^{fpc} = -\gamma^{fpc}N\pi a^2$. The values of γ^{fpc} are related to the values of γ_∞^{fpc} reported in the inset to Fig. 3 as a function of PEG molecular weight. Following the same approach of eqn (6), let us consider the total free energy for a layer of total area δA saturated by $\Phi\delta A/\pi R_0^2$ ideal polymers (at 2-D close-packing, $\Phi \approx 0.91$). The corresponding interfacial tension is $\gamma_\infty^{fpc} = -F_{total}/\delta A = -\Phi\Delta F^{fpc}/\pi R_0^2 + (1-\Phi)\gamma_0$. Replacing ΔF^{fpc} this reads

$$\gamma_\infty^{fpc} = \gamma_0 - \Phi\left(\gamma_0 - \frac{Na^2}{R_0^2}\gamma^{fpc}\right), \quad (8)$$

for the free polymer. Using $\gamma^p = 19$ mN m^{-1} and ($\gamma_0 = 53.12$ mN m^{-1}) and eqn (7) with the model parameters a, l_p previously established, we are in excellent agreement with the measured data for all molecular weights (inset of Fig. 3).

The predictions for the size σ of the PEG–coated NPs in water are also in reasonable agreement with the R_h values quoted in Table 1 using the specified core radii C and Σ as reported in Table 2. Assuming Σ as a weakly increasing function of M_w is consistent with preliminary experimental evidence (see Section 2.1.1). Such result is a consequence of adsorbing the polymer in a fully collapsed state on a highly curved

‖ For a particle to be considered *at the interface*, we assume $|z^{eq}| \leq C$.

** We emphasize that the following discussion is not dependent on this particular choice of σ_0 but is valid for any chosen effective size at the interface.

†† However, as long as $\phi \ll 1$, a scaling analysis can be trivially performed for $R_i^{eq} \ll C$ and $R_i^{eq} \gg C$, corresponding to the limiting cases of a planar brush and non–tethered chains. Interactive online facility available at http://www.complexfluids.ethz.ch/colloids

Table 2 Results from the Flory–type approach for core radii $C = 2.1$ and 4.8 nm, employing model parameters $a = 0.32$ nm, $l_p = 2a$, $\tau_1 = 0.13$ and $\tau_2 = -0.2$. R_0 is the undisturbed PEG radius of gyration; R_i^{eq} is the brush height in solvent i; Σ is the mean surface area per PEG chain; n is the total number of PEG chains within the shell of a single NP; γ_∞^{fpc} is the asymptotic long time-surface tension of free PEG at the interface; σ is the equilibrium core+shell radius to be compared with the hydrodynamic radii in Table 1; z^{eq} is the displacement of the core center from the interfacial plane into solvent 1; σ_0 the effective core+shell radius within the interfacial plane; ΔE the binding energy for a single NP;γ_∞ is the interfacial tension as calculated from eqn (5, 6); γ_∞/γ_0 can be directly compared with the long-time values of γ' in Fig. 2

C	M_w/kDa	N	R_0/nm	γ_∞^{fpc}/mN m^{-1}	Σ/a^2	n	R_1^{eq}/nm	R_2^{eq}/nm	σ/nm	z^{eq}/nm	σ_0/nm	$\Delta E/k_BT$	γ_∞/mN m^{-1}	γ_∞/γ_0
2.1	1.5	35	1.39	36.5	2	271	3.18	2.82	5.28	1.29	4.65	−643	25.7	0.48
2.1	5	115	2.72	32.3	2.5	216	6.82	5.22	8.92	1.9	6.91	−1705	27.7	0.52
2.1	10	230	3.9	31.5	5	108	8.94	5.58	11.04	1.91	8.14	−2419	29.5	0.56
4.8	1.5	35	1.39	36.5	2	1414	3.95	3.66	8.75	2.83	7.68	−1501	29.8	0.56
4.8	5	115	2.72	32.3	2.5	1131	8.91	7.44	13.71	4.52	9.78	−3274	32.4	0.61
4.8	10	230	3.9	31.5	5	565	11.65	8.24	16.45	4.58	11.39	−4629	32.8	0.62

surface. This approach, however, underestimates the hydrodynamic radii for the low molecular weight PEG particles (M_w = 1.5 kDa), even assuming the surface area per polymer to be $\Sigma \simeq a^2$. In this respect the deviations are most likely stemming from neglecting important factors in the conformation and density profile of the brushes arising from the topology of the NP surface (*e.g.* high curvature and nanoscale roughness). Finally, in order to calculate the interfacial quantities of interest as ΔE from eqn (5) or the surface tension γ_∞ from eqn (6), the solvent quality τ_2 has to be specified. Table 2 summarizes these values for a simple choice, $\tau_2 = -0.2$.‡‡ By looking at the values of the trapping energy at the interface we immediately see that they are much larger than the highest $|\Delta E_0| = 100 k_B T$ used in the numerical simulations. As commented in Section 2.2 this calls for a refinement of the interaction potential for more detailed studies, but at the same time enforces the arguments by which our experiments are described by irreversible trapping at the interface. Moreover we see that the Flory model is able to yield values of the saturation interfacial tension which are in the range of the data in Fig. 2. However, the model predicts a weak dependence of γ_∞ on the PEG M_w which is not observed in the experiments. Once more, these minor differences can be expected given the strong approximations made in the model which does not take into account the real $\Sigma(M_w)$, the details of brush properties and the presence of polydispersity in the particle sizes.

These observations are further explored in Fig. 11 where three relevant energy differences are reported as a function σ and τ_2. $F(z^{eq})+\gamma_0\pi(C + \bar{R}_{eq})^2$is the free energy difference at the interface between a coated NP and "naked" one with the same size. We observe that the addition of a polymer shell rapidly makes interfacial adsorption more energetically favorable as a function of σ; moreover, for solvents 2 of higher quality, having a polymer brush is also energetically beneficial due to positive solvation contributions. $F(z^{eq}) - F(0)$ represents the error one makes in calculating the free energy by assuming a fixed particle at $z = 0$ and neglecting the energy penalty paid by the polymer shell exposed to solvent 2. We observe, as one would intuitively expect, that this difference rapidly increases with σ for poor solvents, while the $z = 0$ approximation is accurate for $\tau_1 \approx \tau_2$ and/or small σ. *i.e.* low PEG M_w for a fixed core size. Finally, we note that solvent quality strongly affects how ΔE scales with particle size σ. For $\tau_1 \approx \tau_2$ one has $z^{eq} \approx 0$ and thus $\sigma \approx \sigma_0$ which as a consequence gives $\Delta E \approx -\gamma_0\sigma^2$, as it can be observed at the front of Fig. 11. This quadratic dependence is consistent with the observations reported for hard, "naked" particles;[28,54] in this regime, the behavior of our coated core-shell NPs is well described by an effective representation which neglects the actual role of the polymer shell in the energy balance. However, for poor solvents, the quadratic dependence is lost due to the fact that the contributions coming from the solvation of each portion of the shells exposed to the different solvents become increasingly different and σ is no longer describing the particle size at the interface. The details of $\Delta E(\sigma)$ depend on the specific choices of the parameters in the Flory model (*e.g.* $\Sigma(M_w)$), but it is anyway worth noting that the NP behavior becomes qualitatively different.

‡‡ The results for γ_∞ are anyway only weakly dependent on the precise value of τ_2.

2.4 Discussion

The combination of experimental data and numerical and modeling results lends itself to the discussion of several interesting issues. It is a noteworthy fact that our very simple

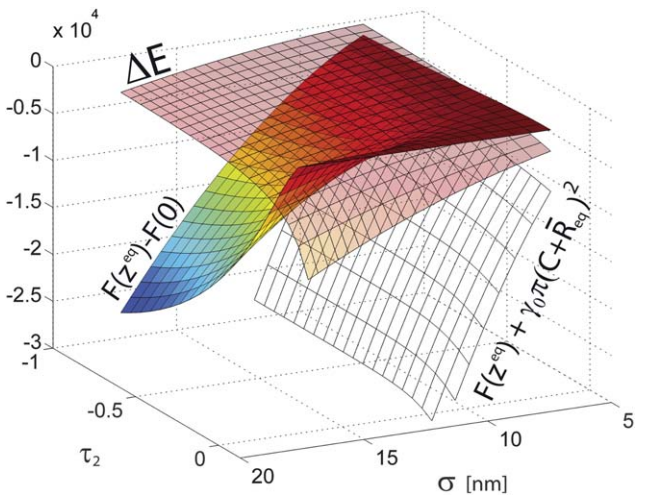

Fig. 11 Three relevant energy differences as a function σ and τ_2 for core-shell NPs. The values of τ_2 terminate at $0.13 = \tau_1$. ΔE represents the trapping energy at the interface; $F(z^{eq}) - F(0)$ represents the error made in calculating the free energy assuming a particle forcefully centered at the interface; $F(z^{eq}) + \gamma_0\pi(C + \bar{R}_{eq})^2$ is the free energy difference at the interface between a coated NP and "naked" one the same hydrodynamic radius σ.

simulation approach reproduces several qualitative features of our experiments and also confirms other experimental observations. In particular the occurrence of size selection at interfaces has been previously observed experimentally in the $\Delta E_0 = 3–6k_BT$ range for CdSe NPs, where the larger ones are preferentially adsorbed at the expenses of the smaller ones.[35] The structure of the interfacial assembly also resembles the data reported from X-ray reflectivity measurements of 3 and 5 nm CdSe NPs at the water/toluene which highlight a highly dense, liquid-like monolayer.[69] Moreover, the numerical study also suggests that cooperative processes become relevant for the adsorption kinetics. In this respect, the soft repulsion and the stability against aggregation provided by the thick PEG shells appear to be key ingredients in the unique manifestation of plateaus in the adsorption kinetics. The absence of the former and the presence of attraction and aggregation at the interface is bound to create a dense percolating particle network in which collective rearrangements and thus the adsorption kinetics are frozen.[70]

The knowledge on the individual NP adsorption behavior gained with our simple Flory model is also remarkable. The main conclusion of the modeling approach lies in the acknowledgement that the adsorption energy is dominated by the solvation of the polymer shell. As a result a non-quadratic scaling of the trapping energy for core-shell NPs is predicted away from neutral solvation conditions as opposed to the case of "naked" particles.[28,54] This fact stems from the complex and unique interplay between the reduction of the interfacial area between the two liquids when a NP sits at the interface and the free energy of the polymer brushes exposed to the two solvents as a function of polymer molecular weight and solvent quality. As a consequence, away from the conditions of equally good solvents, the particle is not centered at the interface and two separate length scales develop and determine the adsorption and the interactions between NPs at the interface. In particular, the three-dimensional character of the problem can no longer be neglected and we need one length scale σ which determines excluded volume interactions and establishes core-to-core separations and another one σ_0 which takes into account the effective particle size at the interface. The excluded volume interactions, and thus inter-particle separation, are not necessarily determined at the interface plane, as for steric hindrance between icebergs floating on water. Conversely, σ_0 will determine viscous forces and motion of the NPs at the interface.[71] These facts can be implemented in the numerical simulations, especially upon gaining more detailed experimental information on the polymer grafting density as a function of M_w and of the conformation of the NPs at the interface, for instance by employing *in situ* X-ray reflectometry. In this case, the knowledge of the shell solvation and polymer density profile could be used as an input parameter to obtain an accurate interaction potential for the numerical simulations and it could also be explicitly used in our Flory-model to estimate the effect of solvent quality, polymer molecular weight and core radius.

Finally, due to the evidence of very large trapping energies at the interface, it is necessary to clarify the nature of the measured interfacial tension γ. Following the arguments presented by Clegg and co-workers,[72] this quantity is indeed conceptually different from the "classical" interfacial tension defined for soluble, surface-active molecules, *e.g.* surfactants and lipids. Soluble molecules at the interface coexist in thermodynamical equilibrium with others in the bulk and can thus adsorb to and desorb from the interface determining an equilibrium surface coverage and consequently an equilibrium interfacial tension which is independent of interface area but which depends on the bulk concentration. The situation is different for our NPs; given the large ΔE, particles in practice do not desorb once adsorbed and the surface coverage keeps growing until a saturated monolayer is formed, as also confirmed by our numerical simulations. Therefore the asymptotic long-time, steady state values of the interfacial tension become independent of the bulk concentration and what is measured in a tensiometry experiment is then an "effective" interfacial tension which is a direct measure of the number of adsorbed particles per unit area times ΔE, as presented in eqn (6). As seen in Section 2.2, the reversibility of particle binding plays also a fundamental role on the kinetics of the adsorption.

3 Experimental

3.1 Material and methods

3.1.1 PEG-iron oxide nanoparticles

3.1.1.1 Materials. $Fe(ac)_2$ (batch 517933, Lot 03901JJ, purity $\geq$ 99.99%), NaCl, KSO_4 and *N*-morpholinopropane sulfunic acid (MOPS) were purchased from Sigma-Aldrich, DOPA, from Acros and PEG(1.5)-NHS, PEG(5)-NHS and PEG(10)-NHS from Jemkem. nitroDOPA was synthesized adapting the protocol reported by Napolitano *et al.*[73] by exchanging dopamine with DOPA.[48] PEG-nitroDOPA was synthesized as described previously.[48]

3.1.1.2 Synthesis and stabilization. Iron oxide cores with radii between 2 and 5 nm were synthesized by a non-aqueous non-gel method. In brief, 1 mmol $Fe(ac)_2$ was dissolved in 5 ml benzylalcohol. The dispersion was heated to 70 °C using an oil bath and kept at this temperature for 1 h to dissolve the precursor. Using the oil bath as an energy source, NPs were nucleated and grown for 24 h under constant magnetic stirring at temperatures between 150 and 180 °C, depending on the targeted core size. NPs were washed twice with ethanol. As-synthesized NPs were stabilized with PEG-nitroDOPA. 6 mg PEG nitroDOPA was dissolved in 0.5 ml ethanol before 5 mg iron oxide NPs dispersed in ethanol at a NP concentration of $\simeq$ 10 mg ml^{-1} were added. PEG-nitroDOPA was adsorbed on iron oxide NPs for 24 h at 50 °C under constant mechanical stirring (Thermomixer comfort, Vaudaux-Eppendorf, Switzerland). Stabilized nanoparticles were purified by dialysis and Sephadex column separation (Sephadex G-75). Purified NPs were freeze-dried and dispersed in Millipore water (R = 18.2 M Ω, TAC $\leq$ 6 ppb) at a concentration of 1 mmol.

3.1.2 Pendant drop tensiometry. PDT experiments were performed with a drop shape analysis system (DSA100, Krüss, Germany). Droplets of 30 μl of the aqueous NP suspension (in MilliQ water, R = 18.2 Ω, TAC $\leq$ 6 ppb) immersed in the non-polar phase (n-decane, 99%, Sigma- Aldrich) were produced at

the tip of a stainless steel needle (diameter 1.85 mm) at a rate of 200 μl min^{-1} at room temperature and imaged with a CCD camera as a function of time. At such formation rates in n-decane inertia effects do not play a significant role; *i.e.* oscillations and drift in the droplet profile are absent. The droplet profile was detected automatically with an analysis software (DSA3, Krüss) and fitted with the Laplace–Young equation to obtain the interfacial tension (γ) as a function of time; the accuracy in determining γ from each image is 0.1 mN/m. Experiments were normally split up into two-three parts: an initial section during which images were taken at a high frame rate (12.5 Hz) and a second, and occasionally third, one where images were grabbed for longer times at lower rates (0.25 Hz and 0.025Hz, respectively). In this way both the fast initial adsorption dynamics and the long-time evolution were captured. Over the time scale of seconds, the measured values of γ were within ± 0.3 mN m^{-1} from the average value. The n-decane was typically used as received but in order to get rid of surface-active molecules prior to the experiments, several aqueous droplets were passed through the oil phase to sequester the impurities and the measurements were started only when the values of γ were within a 0.5 mN m^{-1} tolerance over a 3 min time window. Both the short- and long-time measurements were repeated for consistency and to detect any presence of drift due to contamination. At an initial stage we also tried purifying the n-decane through a basic alumina column[51] but saw no appreciable differences with the procedure described above. Moreover the purified n-decane suffered from environmental contaminations and deteriorated again over days and weeks, while our procedure allows for cleaning only the small volume needed for the PDT measurements ($\simeq$ 5 ml).

3.1.3 Quartz crystal microbalance with dissipation. QCM-D measurements were performed on a Q-sense E4 instrument (Q-Sense, Sweden). 5 MHz AT-cut Au-coated QCM-D crystals (Q-Sense, Sweden) were coated with a 40 nm thick Ti film by evaporation at a rate of 2 Å s^{-1} (Univex 500, Oerlikon Leybold Systems). The metal for evaporation was obtained from Unaxis (Switzerland). Immediately before measurements the Ti-coated crystals were oxidized in a UV/ozone chamber (Bioforce, USA) for 30 min to obtain a clean TiO_2 surface for the PEG-nitroDOPA adsorption. The PEG-nitroDOPA adsorption was carried out *ex-situ*; 100 μg ml^{-1} PEG-nitroDOPA solutions were dissolved in MOPS containing 0.6 M K_2SO_4 and 0.6 M NaCl (pH = 6).[57] Adsorption was performed for 4 h at 80 °C. To remove excessive and physisorbed PEG-nitroDOPA, PEG-nitroDOPA coated crystals were subsequently incubated in Millipore water at 25 °C for 24 h. We point out that the high temperatures make it impossible to perform the adsorption *in situ* in the QCM-D measurement cells, while measuring, since a stable baseline cannot be achieved under these conditions.

4 Conclusions

In this paper we have shown a combination of experimental, numerical and theoretical results aimed at deepening our understanding of the adsorption behavior of composite, core-shell NPs at liquid interfaces. Our findings highlight the fact that the presence of a polymer brush on the NP surface leads to a complex behavior, absent for hard objects, in the collective interfacial adsorption kinetics and in the free energy of individual particles at the interface. Concluding, we highlight once more the simplicity of our measurements, simulations and models which nonetheless led to significant new insights. The study of complex objects at liquid–liquid interfaces, like core-shell NPs, is still in its infancy and we therefore expect further rapid advances of the field to take place in the near future.

5 Acknowledgements

The authors acknowledge Prof. N. D. Spencer and Prof. M. Textor for support. LI acknowledges financial support from MC-IEF- 2009-252926. EA and ER acknowledge financial support from COST Action D43. KS and EDG are supported by the SNSF (Grant No. PP002_126483/1). MK is supported by SNSF (Grant No. SCOPES IZ73Z0-128169).

References

1 W. Zhao, M. A. Brook and Y. F. Li, *ChemBioChem*, 2008, **9**, 2363–2371.
2 S. Lal, S. E. Clare and N. J. Halas, *Acc. Chem. Res.*, 2008, **41**, 1842–1851.
3 C. Sun, J. S. H. Lee and M. Q. Zhang, *Adv. Drug Delivery Rev.*, 2008, **60**, 1252–1265.
4 M. J. Pittet, F. K. Swirski, F. Reynolds, L. Josephson and R. Weissleder, *Nat. Protoc.*, 2006, **1**, 73–79.
5 M. Namdeo, S. Saxena, R. Tankhiwale, M. Bajpai, Y. M. Mohan and S. K. Bajpai, *J. Nanosci. Nanotechnol.*, 2008, **8**, 3247–3271.
6 J. H. Lee, Y. M. Huh, Y. Jun, J. Seo, J. Jang, H. T. Song, S. Kim, E. J. Cho, H. G. Yoon, J. S. Suh and J. Cheon, *Nat. Med.*, 2006, **13**, 95–99.
7 A. C. Balazs, T. Emrick and T. P. Russell, *Science*, 2006, **314**, 1107–1110.
8 J. Xie, C. Xu, N. Kohler, Y. Hou and S. Sun, *Adv. Mater.*, 2007, **19**, 3163.
9 M. F. Bedard, D. Braun, G. B. Sukhorukov and A. G. Skirtach, *ACS Nano*, 2008, **2**, 1807–1816.
10 D. A. Gorin, S. A. Portnov, O. A. Inozemtseva, Z. Luklinska, A. M. Yashchenok, A. M. Pavlov, A. G. Skirtach, H. Mohwald and G. B. Sukhorukov, *Phys. Chem. Chem. Phys.*, 2008, **10**, 6899–6905.
11 X. Zhao, J. Kim, C. A. Cezar, N. Huebsch, K. Lee, K. Bouhadir and D. J. Mooney, *Proc. Natl. Acad. Sci. U. S. A.*, 2010, **108**, 67–72.
12 E. Amstad, J. Kohlbrecher, E. Müller, T. Schweizer, M. Textor and E. Reimhult, *Nano Lett.*, 2011, **11**, 1664–1670.
13 A. S. Angelatos, B. Radt and F. Caruso, *J. Phys. Chem. B*, 2005, **109**, 3071–3076.
14 M. Grzelczak, J. Perez-Juste, P. Mulvaney and L. M. Liz-Marzan, *Chem. Soc. Rev.*, 2008, **37**, 1783–1791.
15 S. C. Glotzer and M. J. Solomon, *Nat. Mater.*, 2007, **6**, 557–562.
16 K. J. M. Bishop, C. E. Wilmer, S. Soh and B. A. Grzybowski, *Small*, 2009, **5**, 1600–1630.
17 M. Grzelczak, J. Vermant, E. M. Furst and L. Liz-Marzan, *ACS Nano*, 2010, **4**, 3591–3605.
18 A. Boeker, J. He, T. Emrick and T. P. Russell, *Soft Matter*, 2007, **3**, 1231–1248.
19 H. W. Duan, D. Y. Wang, N. S. Sobal, M. Giersig, D. G. Kurth and H. Mohwald, *Nano Lett.*, 2005, **5**, 949–952.
20 Y. Lin, H. Skaff, A. Boker, A. D. Dinsmore, T. Emrick and T. P. Russell, *J. Am. Chem. Soc.*, 2003, **125**, 12690–12691.
21 H. Skaff, Y. Lin, R. Tangirala, K. Breitenkamp, A. Boker, T. P. Russell and T. Emrick, *Adv. Mater.*, 2005, **17**, 2082.
22 J. T. Russell, Y. Lin, A. Boker, L. Su, P. Carl, H. Zettl, J. B. He, K. Sill, R. Tangirala, T. Emrick, K. Littrell, P. Thiyagarajan, D. Cookson, A. Fery, Q. Wang and T. P. Russell, *Angew. Chem., Int. Ed.*, 2005, **44**, 2420–2426.
23 E. Glogowski, R. Tangirala, J. B. He, T. P. Russell and T. Emrick, *Nano Lett.*, 2007, **7**, 389–393.

24 P. Arumugam, D. Patra, B. Samanta, S. S. Agasti, C. Subramani and V. M. Rotello, *J. Am. Chem. Soc.*, 2008, **130**, 10046.
25 H. Xia and D. Wang, *Adv. Mater.*, 2008, **20**, 4253–4256.
26 B. S. Binks and T. S. Horozov, *Colloidal particles at liquid interfaces*, Cambridge University Press, Cambridge, 2006.
27 F. Bresme and M. Oettel, *J. Phys.: Condens. Matter*, 2007, **19**, 413101.
28 P. Pieranski, *Phys. Rev. Lett.*, 1980, **45**, 569–572.
29 F. Reincke, S. G. Hickey, W. K. Kegel and D. Vanmaekelbergh, *Angew. Chem., Int. Ed.*, 2004, **43**, 458–462.
30 F. Reincke, W. K. Kegel, H. Zhang, M. Nolte, D. Y. Wang, D. Vanmaekelbergh and H. Mohwald, *Phys. Chem. Chem. Phys.*, 2006, **8**, 3828–3835.
31 Y. K. Park, S. H. Yoo and S. Park, *Langmuir*, 2007, **23**, 10505–10510.
32 Y. K. Park and S. Park, *Chem. Mater.*, 2008, **20**, 2388–2393.
33 M. Oettel and S. Dietrich, *Langmuir*, 2008, **24**, 1425–1441.
34 F. Bresme, H. Lehle and M. Oettel, *J. Chem. Phys.*, 2009, **130**, 214711.
35 Y. Lin, H. Skaff, T. Emrick, A. D. Dinsmore and T. P. Russell, *Science*, 2003, **299**, 226–229.
36 H. W. Duan, D. A. Wang, D. G. Kurth and H. Mohwald, *Angew. Chem., Int. Ed.*, 2004, **43**, 5639–5642.
37 J. B. He, Z. W. Niu, R. Tangirala, J. Y. Wan, X. Y. Wei, G. Kaur, Q. Wang, G. Jutz, A. Boker, B. Lee, S. V. Pingali, P. Thiyagarajan, T. Emrick and T. P. Russell, *Langmuir*, 2009, **25**, 4979–4987.
38 K. A. Tay and F. Bresme, *J. Am. Chem. Soc.*, 2006, **128**, 14166–14175.
39 A. S. Almusallam, *Phys. Chem. Chem. Phys.*, 2008, **10**, 3099–3107.
40 L. Isa, E. Amstad, M. Textor and E. Reimhult, *Chimia*, 2010, **64**, 145–149.
41 R. Weissleder, D. D. Stark, B. L. Engelstad, B. R. Bacon, C. C. Compton, D. L. White, P. Jacobs and J. Lewis, *Am. J. Roentgenol.*, 1989, **152**, 167–173.
42 J. H. Lee, Q. Wu and W. Park, *Opt. Lett.*, 2009, **34**, 443–445.
43 E. Amstad, S. Zurcher, A. Mashaghi, J. Y. Wong, M. Textor and E. Reimhult, *Small*, 2009, **5**, 1334–1342.
44 C. J. Xu, K. M. Xu, H. W. Gu, R. K. Zheng, H. Liu, X. X. Zhang, Z. H. Guo and B. Xu, *J. Am. Chem. Soc.*, 2004, **126**, 9938–9939.
45 J. Xie, C. Xu, N. Kohler, Y. Hou and S. Sun, *Adv. Mater.*, 2007, **19**, 3163.
46 H. W. Gu, Z. M. Yang, J. H. Gao, C. K. Chang and B. Xu, *J. Am. Chem. Soc.*, 2005, **127**, 34–35.
47 J. H. Gao, G. L. Liang, J. S. Cheung, Y. Pan, Y. Kuang, F. Zhao, B. Zhang, X. X. Zhang, E. X. Wu and B. Xu, *J. Am. Chem. Soc.*, 2008, **130**, 11828–11833.
48 E. Amstad, T. Gillich, I. Bilecka, M. Textor and E. Reimhult, *Nano Lett.*, 2009, **9**, 4042–4048.
49 E. Amstad, A. U. Gehring, H. Fischer, V. V. Nagaiyanallur, G. Haehner, M. Textor and E. Reimhult, *J. Phys. Chem. C*, 2011, **115**, 683–691.
50 D. B. Thiessen, D. J. Chione, C. B. McCreary and W. B. Krantz, *J. Colloid Interface Sci.*, 1996, **177**, 658–665.
51 A. Goebel and K. Lunkenheimer, *Langmuir*, 1997, **13**, 369–372.
52 E. Amstad, L. Isa and E. Reimhult, *Chimia*, 2010, **64**, 826–826.
53 S. Kutuzov, J. He, R. Tangirala, T. Emrick, T. P. Russell and A. Boker, *Phys. Chem. Chem. Phys.*, 2007, **9**, 6351–6358.
54 K. Du, E. Glogowski, T. Emrick, T. P. Russell and A. D. Dinsmore, *Langmuir*, 2010, **26**, 12518–12522.
55 M. Rodahl, F. Hook, A. Krozer, P. Brzezinski and B. Kasemo, *Rev. Sci. Instrum.*, 1995, **66**, 3924–3930.
56 M. T. Muller, X. P. Yan, S. W. Lee, S. S. Perry and N. D. Spencer, *Macromolecules*, 2005, **38**, 3861–3866.
57 B. Malisova, S. Tosatti, M. Textor, K. Gademann and S. Zurcher, *Langmuir*, 2010, **26**, 4018–4026.
58 E. Reimhult, C. Larsson, B. Kasemo and F. Hook, *Anal. Chem.*, 2004, **76**, 7211–7220.
59 F. Hook, B. Kasemo, T. Nylander, C. Fant, K. Sott and H. Elwing, *Anal. Chem.*, 2001, **73**, 5796–5804.
60 D. Frenkel and B. Smit, *Understanding Molecular Simulation*, Academic press, 2002.
61 M. Allen and D. Tildesley, *Computer Simulation of Liquids*, Oxford Science Publications, 1987.
62 P.-G. De Gennes, *Scaling Concepts in Polymer Physics*, Cornell University Press, New York, 1988.
63 M. Kröger, O. Peleg and A. Halperin, *Macromolecules*, 2010, **43**, 6213–6224.
64 A. Halperin, M. Kröger and E. Zhulina, *Macromolecules*, 2011, **44**, 3622–3638.
65 R. M. and R. H. Colby, *Polymer Physics*, Oxford University Press, Oxford, England, 2003.
66 L. Livadaru, R. R. Netz and H. J. Kreuzer, *J. Chem. Phys.*, 2003, **118**, 1404–1416.
67 A. Halperin and M. Kröger, *Langmuir*, 2009, **25**, 11621–11634.
68 K. Devanand and J. C. Selser, *Macromolecules*, 1991, **24**, 5943–5947.
69 Y. Lin, A. Boker, H. Skaff, D. Cookson, A. D. Dinsmore, T. Emrick and T. P. Russell, *Langmuir*, 2005, **21**, 191–194.
70 E. Sanz, K. A. White, P. S. Clegg and M. E. Cates, *Phys. Rev. Lett.*, 2009, **103**, 255502.
71 T. M. Fischer, P. Dhar and P. Heinig, *J. Fluid Mech.*, 2006, **558**, 451–475.
72 P. S. Clegg, E. M. Herzig, A. B. Schofield, S. U. Egelhaaf, T. S. Horozov, B. P. Binks, M. E. Cates and W. C. K. Poon, *Langmuir*, 2007, **23**, 5984–5994.
73 A. Napolitano, M. Dischia, C. Costantini and G. Prota, *Tetrahedron*, 1992, **48**, 8515–8522.